



Cite this: *RSC Adv.*, 2024, **14**, 26788

## Pristine and aurum-decorated tungsten ditellurides as sensing materials for VOCs detection in exhaled human breath: DFT analysis

Rabia Gilani,<sup>a</sup> Saleh S. Alarfaji,<sup>b</sup> Kashif Nadeem,<sup>c</sup> Ashir Saeed<sup>c</sup> and Muhammad Isa Khan  <sup>\*ac</sup>

In this research, we employed density functional theory (DFT) to evaluate the sensing capabilities of transition metal-decorated two-dimensional WTe<sub>2</sub> TMDs nanosheets toward VOCs such as (acetone, ethanol, methanol, toluene, and formaldehyde) that are exhaled in human breath and can serve as potential biomarkers for detecting specific physiological disorders and also gases interfering in exhaled breath (CO<sub>2</sub> and H<sub>2</sub>O) detection. Au can be physically decorated onto the surface of WTe<sub>2</sub>. We analyzed the density of states (DOS), adsorption energy, charge transfer, and sensing behavior. The pristine WTe<sub>2</sub> monolayer, exhibiting a semiconductor characteristic with a band gap of 0.63 eV, transitions to a metallic state upon Au-decoration, due to its actively stable nature and promising negative adsorption energy value, it triggers the emergence of novel states within the DOS. Computed adsorption energies of VOCs range from -0.08 to -0.57 eV, with greater interaction distances confirming the physisorption behavior of these VOCs biomarkers on Au-WTe<sub>2</sub>. Ethanol displays greater sensitivity compared to other considered VOCs. Au-WTe<sub>2</sub> exhibits promising potential as a viable option for detecting VOCs in breath analysis applications at room temperature, owing to its excellent adsorption capabilities and sensitivity. Overall, our results highlight aurum-decorated tungsten ditelluride's potential as an efficient nano-sensor for detecting VOCs associated with early-stage lung cancer diagnoses.

Received 22nd June 2024  
 Accepted 14th August 2024

DOI: 10.1039/d4ra04569f  
[rsc.li/rsc-advances](http://rsc.li/rsc-advances)

### 1. Introduction

Today, detecting over 870 types of volatile organic compounds (VOCs) in human breath is crucial due to the rise in indoor air pollution, which poses risks to both the environment and human health.<sup>1-4</sup> VOCs, due to their low binding to solid surfaces and non-reactivity, can aid in the early identification of ailments, providing a non-invasive and speedy diagnosis method.<sup>2,5</sup> Exhaled breath primarily consists of nitrogen (78.04%), oxygen (16%), carbon dioxide (4-5%), and hydrogen, with ammonia concentrations ranging from 0.5 to 2 ppm and carbon monoxide concentrations ranging from 0 to 6 ppm.<sup>6</sup> Breath analysis is a diagnostic tool used to identify significant diseases like liver cirrhosis, multiple sclerosis, skin conditions, central nervous system disorders, and various types of cancer.<sup>7</sup> Acetone concentration in human breath is a key indicator of diabetes, with concentrations exceeding 1.7 ppm in type 2 and 2.2 ppm in type 1

diabetics. Formaldehyde, a carcinogenic, irritant, and toxic substance, can also cause respiratory diseases.<sup>8</sup> Dongzhi Zhang *et al.* have made significant strides in sensor technology, exploring innovative materials and mechanisms for self-powered, high-performance detection of formaldehyde, hydrogen, and tactile sensing in wearable applications. Their investigation focuses on a room-temperature formaldehyde sensor constructed from an MXene/Co<sub>3</sub>O<sub>4</sub> composite and a ZnO/MXene nanowire array piezoelectric nanogenerator. The study examines the sensor's self-powering capability and the synergistic interactions between MXene and Co<sub>3</sub>O<sub>4</sub>, highlighting its potential for wearable applications.<sup>9</sup> They investigated at 300 °C, a new sandwich-structured hydrogen gas sensor made of Ag nanoparticles, SnO<sub>2</sub>, and an electron supply layer that exhibits remarkable performance. It has long-term stability, a low detection limit, great selectivity, and quick reaction/recovery times. Strong adsorption energy and hybridization between H<sub>2</sub> and SnO<sub>2</sub> orbitals are responsible for the sensor's efficacy in detecting hydrogen, which makes it valuable for forecasting thermal runaway in batteries and also introduces a flexible triboelectric nanogenerator sensor for wireless, self-powered tactile sensing, and intelligent material recognition in wearable electronics and smart sensing. They also developed a wearable triboelectric nanogenerator (S-TENG) with stability, large-scale detection, and energy harvesting, making it ideal for electronic devices and self-

<sup>a</sup>Institute of Physics, Bagdad ul Jadeed, Islamia University of Bahawalpur, Bahawalpur, Pakistan. E-mail: rabiagilani03@gmail.com; muhammad.isa@iub.edu.pk

<sup>b</sup>Department of Chemistry, Faculty of Science, King Khalid University, P. O. Box 9004, Abha 61413, Saudi Arabia. E-mail: ssalarvagi@kku.edu.sa

<sup>c</sup>Department of Physics, Rahim Yar Khan Campus, Islamia University of Bahawalpur, Bahawalpur, Pakistan. E-mail: kashif90nadeem@gmail.com; ashir.saeed@iub.edu.pk



powered wearable sensors.<sup>10–12</sup> Shuaipeng Wang *et al.*<sup>13</sup> introduced a novel cantilever array biosensor to detect biomarkers for liver cancer, while Nir Peled *et al.*<sup>14</sup> Lung cancer research focuses on volatile emissions linked to cancer-specific mutations, highlighting the need for nanostructured chemiresistive gas sensors for rapid, sensitive, and cost-effective detection.<sup>15</sup> Yuvaraj *et al.* investigated  $\text{Sc}_2\text{CO}_2$  MXene nanosheets that detected volatile organic compounds in human breath, showing high sensitivity to acetonitrile and potential for room-temperature illness sensors.<sup>16</sup> Transition Metal Di-chalcogenide (TMD), a 2-D material, is widely used as a sensing material in biosensors.<sup>17</sup> Molybdenum and tungsten dichalcogenides are well-regarded 2D layered materials because of their distinctive chemical and physical properties.<sup>18</sup> TMD, including  $\text{MoSe}_2$ ,  $\text{WS}_2$ ,  $\text{MoS}_2$ , and  $\text{MoTe}_2$ , are two-dimensional materials with few layers with potential applications in energy storage, catalysis, optoelectronics, and microelectronics.<sup>19–22</sup>  $\text{WTe}_2$ , with superconductivity and topological states, is a promising candidate for studying topological superconductivity and its role in quantum computing applications.<sup>23</sup>  $\text{WTe}_2$  is a TMD<sub>C</sub> known for its unique electronic structure and optical properties, with electron mobility exhibiting a pattern of  $\text{WS}_2 < \text{WSe}_2 < \text{WTe}_2$ .<sup>24</sup> Nan Gao *et al.* evaluates the adsorption and sensing capabilities of six VOCs on both pristine and Li-doped F-diamine, suggesting its suitability as a sensor for detecting  $\text{C}_2\text{HCl}_3$ .<sup>25</sup> R. Chandiramouli *et al.* explored the adsorption properties, rapid recovery times, and resistance changes of  $\text{MoSe}_2$  nanosheets when exposed to ML and EL vapor molecules.<sup>26</sup> Hao Cui *et al.* examined the operating conditions of oil-immersed transformers and assesses the potential of Ni-doped  $\text{WTe}_2$  monolayer to improve adsorption and sensing in transformer oil.<sup>27</sup> Zhang *et al.* investigated that the Pd-decorated  $\text{WTe}_2$  monolayer exhibits promising gas sensing capabilities for  $\text{SO}_2$  and  $\text{SOF}_2$ .<sup>28</sup> Xiqian Hu *et al.* explored that Pd-doped  $\text{MoTe}_2$  enhances gas sensing by reducing the band gap, increasing conductivity, and improving adsorption compared to pure  $\text{MoTe}_2$ .<sup>29</sup> Ran Jia *et al.* investigated the adsorption of VOCs in breath, aiming to develop rapid and cost-effective screening methods for early lung cancer detection.<sup>30</sup> In this study, we used DFT to assess the effectiveness of pristine  $\text{WTe}_2$  and Au-decorated  $\text{WTe}_2$  in detecting VOCs in human breath. We analyzed their electronic properties, such as band structure and density of states, ELF, and studied  $\text{WTe}_2$ 's adsorption behavior towards different VOCs, including alcohols, ketones, nitriles, and hydrocarbons. Comparisons with other 2D materials highlighted  $\text{WTe}_2$  superior adsorption capabilities. Hirshfeld charge analysis quantified charge transfer upon VOCs adsorption, while we evaluated gas-sensing performance in terms of recovery time, sensitivity, and selectivity. Additionally, we explored how VOC adsorption affects  $\text{WTe}_2$  work function, suggesting its potential as a work function-based sensor for early disease diagnosis through breath analysis.

## 2. Methods

### 2.1. Calculation methods

The ADF-BAND package was utilized to analyze energy parameters, configuration, gas adsorption, and electronic simulation models using the DFT methodology. Realistic orbital behavior

around the nucleus within the examined structure was accomplished by employing ADF's Slater-type orbitals (STOs).<sup>31,32</sup> The atomic, and electronic wave functions were considered using a triple zeta polarization (TZP) basis set, standard numerical precision, and a non-frozen core approach.<sup>33</sup> Investigation delved into the influence of electron density on ion exchange-correlation energies by employing Perdew–Burke–Ernzerhof (PBE) generalized gradient approximation (GGA).<sup>34</sup> Incorporating van der Waals (vdW) interactions through D3-Grimme correction (DFT-D3) notably enhances the precise depiction of long-range interaction between gas molecules and Au-decorated  $\text{WTe}_2$ .<sup>35</sup> Fully optimized lattice constants and atomic positions were attained using five (05)  $k$ -points. Selection of  $k$ -grid, basis set, and density fitting parameters critically influences numerical accuracy in ADF. These chosen  $k$ -points, derived from Becke's fuzzy cell technique, are pivotal in sampling the Brillouin zone and establishing numerical precision in calculations.<sup>36</sup> Convergence criteria for structure relaxation were set, including energy ( $10^{-5}$  eV), gradient ( $0.02$  eV Å<sup>−1</sup>), and step size ( $10^{-3}$  Å). These criteria were consistently applied to all relaxation processes.<sup>37</sup> The convergence criteria in the ADF-BAND package are designed to ensure the reliability of the results by requiring that iterative calculations reach a stable solution. These criteria typically involve thresholds for changes in total energy, electron density, band structure convergence, and forces. By adhering to these stringent criteria, the package guarantees that the results are accurate, reproducible, and reliable for further analysis.

### 2.2. Analytical methods

The stability of  $\text{WTe}_2$ , a monolayer, decorated with Au, is often assessed using binding energy  $E_b$ , as described by eqn (1).

$$E_b = \text{EWTe}_2/\text{Au} - \text{EWTe}_2 - \text{EAu} \quad (1)$$

In which  $\text{EWTe}_2/\text{Au}$  signify the energy of transition metal (Au) decorated TMDs,  $E_{\text{Au}}$  denotes the energy of aurum metal, and  $E_{\text{WTe}_2}$  signify the energy of the  $\text{WTe}_2$  monolayer. Term adsorption energy  $E_{\text{ads}}$  is used to characterize interaction energy and constancy between VOCs and TMDs, which is as eqn (2):

$$E_{\text{ads}} = E_{\text{total}} - E_{\text{VOC}} - E_{\text{substrate}} \quad (2)$$

where  $E_{\text{total}}$  is the energy of a total adsorbed system and  $E_{\text{VOC}}$  denotes the total energy of the gas molecules and  $E_{\text{substrate}}$  energy of Au- $\text{WTe}_2$ . Hirshfeld analysis was employed concurrently to examine charge transfer ( $\Delta Q$ ) between the target molecule and the adorned surface, as expressed in eqn (3):

$$\Delta Q = Q_2 - Q_1 \quad (3)$$

A positive  $\Delta Q$  signifies an electron donor, while a negative electron-accepting behavior in the target molecule. Conductivity ( $\sigma$ ) and sensitivity of the  $\text{WTe}_2$  base monolayer and adsorption system can be predicted using eqn (4) and (5) based on frontier orbital theory.



$$\sigma = A \times e^{-\frac{E_g}{k_B T}} \quad (4)$$

$$S = \frac{\sigma_{\text{substrate}}}{\sigma_{\text{VOC+substrate}}} - 1 \quad (5)$$

A smaller band gap  $E_g$ , combined with constant  $A$ , Boltzmann constant ( $k$ ), and temperature ( $T$ ), implies higher conductivity at a given temperature. This correlation is crucial for investigating the electrical properties effectively of Au-WTe<sub>2</sub> for gas sensing at different temperatures and  $\sigma_{\text{VOC+substrate}}$  and  $\sigma_{\text{substrate}}$  electrically conductive values of Au-decorated WTe<sub>2</sub> with VOCs, and Au-WTe<sub>2</sub> respectively. Additionally, the ability of the Au-WTe<sub>2</sub> monolayer to recover can be examined through van't Hoff-Arrhenius/transition state theory and is expressed in eqn (6).<sup>38,39</sup>

$$\tau = A^{-1} e^{\frac{E_{\text{ads}}}{k_B T}} \quad (6)$$

$A$ , attempted frequency, is determined to be  $10^{12}$  s<sup>-1</sup>.  $E_{\text{ads}}$  represent adsorption energy,  $k_B$  and  $T$  denote Boltzmann constant, and the sensor's temperature ( $8.6173303 \times 10^{-5}$  eV K<sup>-1</sup>).<sup>25,29,40,41</sup> A valuable approach for gas sensors includes tracking changes in the work function of the sensing substrate. The work function ( $\Phi$ ), calculated as

$$\Phi = V(\Phi) - E_f \quad (7)$$

$V(\Phi)$  represents electrostatic potential relative to vacuum level, and  $E_f$  denotes potential relative to Fermi energy level. Variable  $\Phi$  responds to surface changes induced by gas adsorption.<sup>16,42</sup>

### 3. Results and discussion

#### 3.1 Structural property of pristine and Au-decorated WTe<sub>2</sub>

Firstly, the honeycomb structure of pristine WTe<sub>2</sub> monolayer (WTe<sub>2</sub>-ML) was configured with a supercell of dimensions  $4 \times 4 \times 1$ , housing a total of 16 W atoms and 32 Te atoms with W atoms positioned between two Te sublayers, as illustrated in Fig. 1(a). According to our computations, the lattice constant of the WTe<sub>2</sub> monolayer is determined to be 3.54 Å, the W-Te bond length measures 2.70 Å, and the bond angle is 72.3° is shorter, indicating a smaller atomic radius compared to the previously reported value of 2.76 Å bond length remains consistent after optimization. These values align with a previous theoretical report indicating a lattice constant of 3.6 Å.<sup>43</sup> WTe<sub>2</sub> primarily exists in 2H- and Td-phases, the Td-phase, often referred to as 1T-phase, has received the most research attention. Furthermore, because of its remarkable superconducting features, the T-phase of WTe<sub>2</sub> has garnered interest.<sup>23,44,45</sup> For dynamic stability of WTe<sub>2</sub> phonon dispersion in the reported structure.<sup>46</sup> WTe<sub>2</sub>-ML was optimized to attain relaxed geometric configuration and electronic properties of decorated ad-atom and adsorbed gases.

Notably, decorating with metal elements is an effective strategy to enhance the sensitivity of adsorbent. The adsorption performance of the WTe<sub>2</sub> was enhanced by decorating this with Au atom. For the most stable configuration of Au-WTe<sub>2</sub>, three distinct locations on pristine WTe<sub>2</sub> monolayer surfaces were

examined for ideal locations for VOCs. These positions encompassed the T<sub>w</sub> site positioned over the W atom, the T<sub>Te</sub> site positioned over the Te atom, and the H site located overhead center of the six-membered ring as illustrated in Fig. 1(a). The optimal configuration for Au-decoration on the WTe<sub>2</sub> monolayer is found at the H site, exhibiting the highest interaction strength with  $E_b$  of -8.61 eV which indicates Au-WTe<sub>2</sub> configuration showed superior stability and strong interaction at the H site, with Au decoration forming a bond with three Te atoms with bond lengths of 3.030 Å is illustrated in Fig. 1(b).

The bond length between W and Te atoms was 2.7 Å. The Au atom is adsorbed on the hollow site of WTe<sub>2</sub>. In this structure, the W atoms are sandwiched between the Te atoms, as shown in Fig. 1. The hexagonal structure of WTe<sub>2</sub> has three Te and three W atoms, and only all Te atoms form a bond with Au, with a bond length of 3.030 Å.

#### 3.2 Electronic properties of pristine and Au-decorated WTe<sub>2</sub>

Investigated electronic properties of Au-decorated WTe<sub>2</sub> compared to pure WTe<sub>2</sub> by examining total DOS and projected DOS, as depicted in Fig. 2(a-c). DOS analysis of pristine WTe<sub>2</sub> indicates an absence of states at the Fermi level, suggesting its semiconducting nature with a bandgap of 0.63 eV. Moreover, the TDOS and PDOS curves of Au-WTe<sub>2</sub> shift to a higher energy region after Au decoration. This shift is attributed to the electron-donating behavior of WTe<sub>2</sub>, leading to an improved effective Coulomb potential. Additionally, a transition from semiconducting to metallic behavior is observed. Comparison with the pristine WTe<sub>2</sub> system reveals that Au-decoration introduces novel states, some of which fill the bandgap, transforming the Au-decorated WTe<sub>2</sub> monolayer into a metallic state. Atomic DOS analysis demonstrates significant overlap between Au 5d, 6s orbital, and Te 5p orbital at -1.0 and 1.5 eV, indicating durable orbital interactions between Au and Te atoms. This interaction further contributes to alteration in the electronic states of the Au-decorated WTe<sub>2</sub> system.

In the context of Hirshfeld analysis, Au exhibits a negative charge of -0.211e, acting as an electron acceptor and withdrawing 0.063e from WTe<sub>2</sub>. Conversely, each of the three bonded Te atoms carries a positive charge of 1.276e, demonstrating an electron-donating behavior. W atoms act as electron acceptors, whereas Te atoms act as donors. This highlights the electronegativity of W and Te atoms within a system, along with newly formed Au-Te bonds. Moreover, Au-Te bonds display electron accumulation, confirming the electron-donating property of Te atoms and emphasizing robust orbital interactions in Au-Te bond formation.

We have calculated ELF which is a computational tool used to visualize different degrees of electron localization and the value lies in the range of 0 to 1. Where 0 represents delocalized electrons (metallic behavior), and 1 indicates highly localized electrons (covalent or ionic behavior) also calculation is used to understand chemical bonds and interactions that is illustrated in Fig. 2(d). It provides insights into electron pairs and bonding types through varied colors. Red on WTe<sub>2</sub> indicates strong electron localization associated with covalent or directional



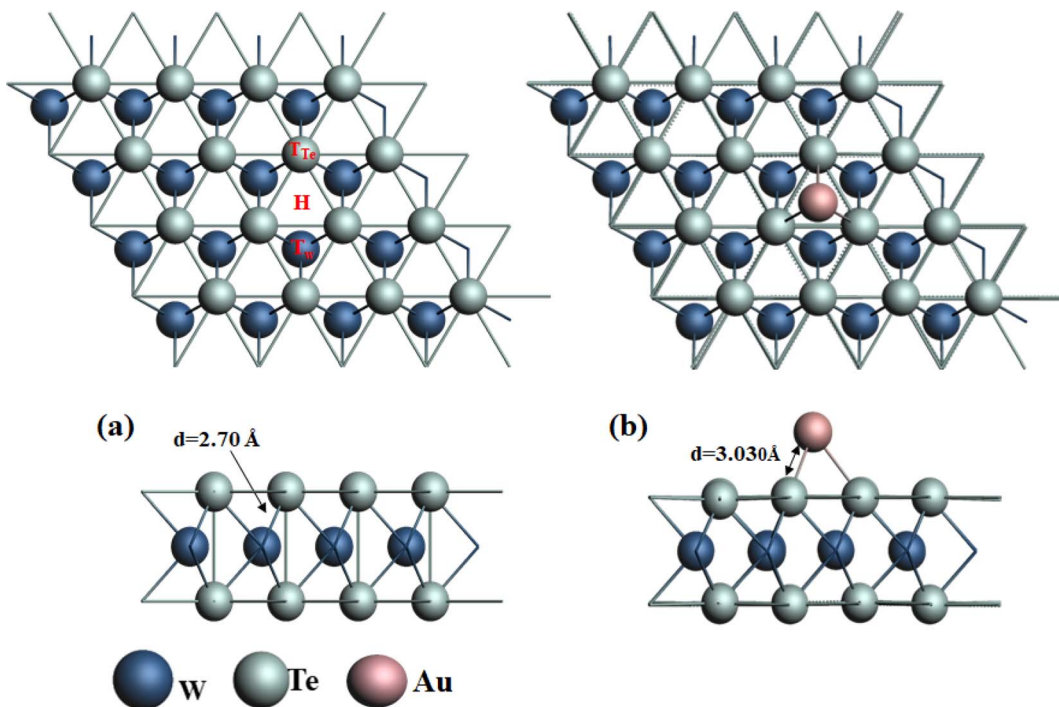


Fig. 1 (a) Geometric structure of pristine  $\text{WTe}_2$  with three typical locations and (b) Au-decorated  $\text{WTe}_2$ .

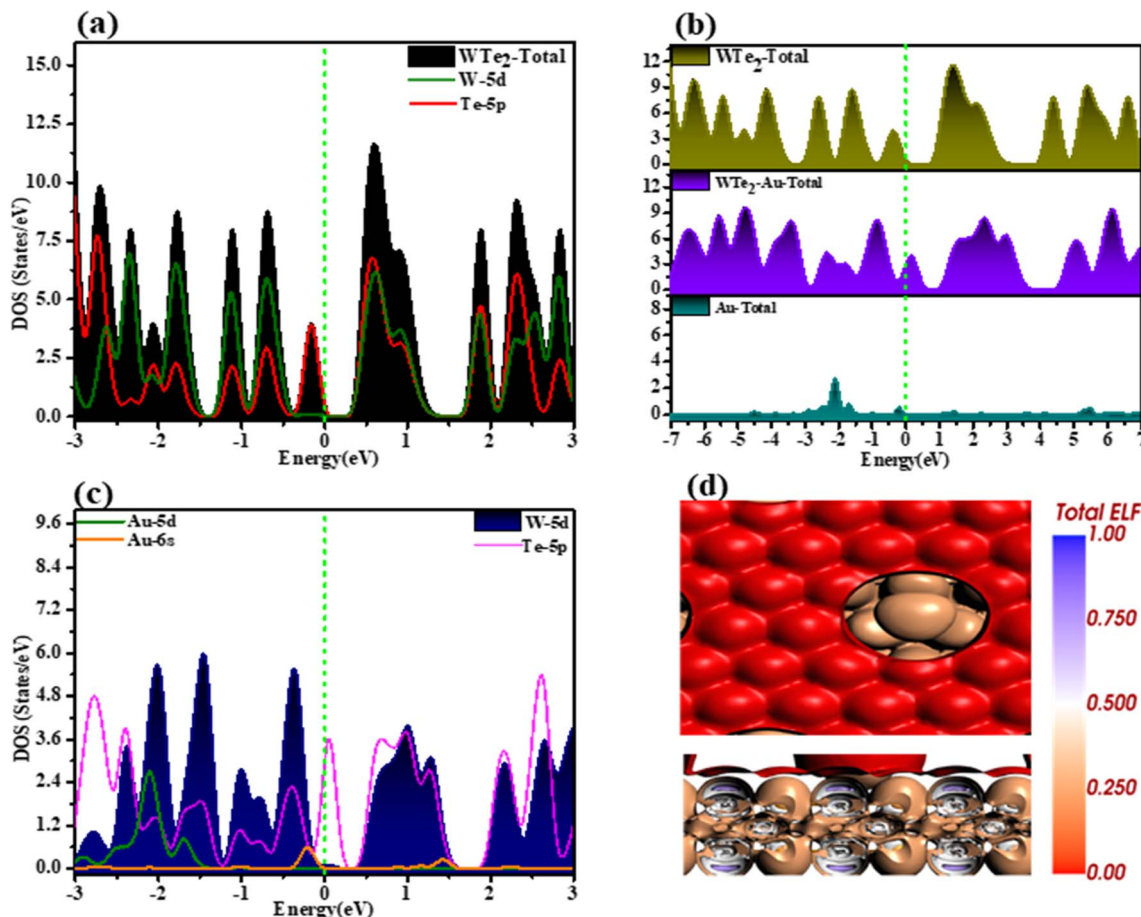


Fig. 2 (a–c) TDOS and PDOD curves of pristine  $\text{WTe}_2$ , Au-decorated  $\text{WTe}_2$ , and green dashed lines are Fermi level, (d) ELF of Au- $\text{WTe}_2$ .

Table 1 Theoretically reviewed ( $E_{\text{ads}}$ ) eV of VOCs with other 2D nano-sensors

Sensing materials	H <sub>2</sub> O	CO <sub>2</sub>	CH <sub>2</sub> O	CH <sub>4</sub> O	C <sub>7</sub> H <sub>8</sub>	C <sub>3</sub> H <sub>6</sub> O	C <sub>2</sub> H <sub>5</sub> OH	References
WTe <sub>2</sub>	<b>-0.01</b>	<b>-0.09</b>	<b>-0.01</b>	<b>-0.10</b>	<b>-0.07</b>	<b>-0.06</b>	<b>-0.08</b>	This work
Au-WTe <sub>2</sub>	<b>-0.28</b>	<b>-0.14</b>	<b>-0.24</b>	<b>-0.11</b>	<b>-0.55</b>	<b>-0.08</b>	<b>-0.57</b>	This work
BC <sub>6</sub> N	—	—	-0.22	—	—	—	-0.37	38
Tellurene-MoS <sub>2</sub>	—	—	—	—	—	-0.32	-0.21	47 and 48
Phosphorus	—	—	—	—	-0.43	—	-0.21	49
MoS <sub>2</sub>	—	—	-0.25	—	—	—	-0.25	50
B <sub>4</sub> C <sub>3</sub>	-0.19	-0.15	-0.19	—	-0.21	—	—	51
N-WS <sub>2</sub>	-0.15	—	—	—	—	—	—	30
Sc <sub>2</sub> CO <sub>2</sub>	-0.44	-0.19	—	—	-0.18	-0.48	-0.59	16

bonds and signifies regions with high electron localization while brown hues on Au suggest lower electron localization characteristic of metallic bonding and indicate specific electron densities that are known for their metallic properties and in the context of WTe<sub>2</sub> sheets, they likely form metallic bonds.

### 3.3. Structures of adsorption and electronic properties of VOCs over Au-decorated WTe<sub>2</sub>

Investigation delves into enduring adsorption, dynamics, and electronic configuration of gases onto pristine WTe<sub>2</sub> and decorated with metal (Au). Results indicate that some gas molecules adsorbed physically on the structure. The adsorption energies of WTe<sub>2</sub> towards gases are classified from higher to lower as follows: CH<sub>4</sub>O > CO<sub>2</sub> > C<sub>2</sub>H<sub>5</sub>OH > C<sub>7</sub>H<sub>8</sub> > C<sub>3</sub>H<sub>6</sub>O > H<sub>2</sub>O, CH<sub>2</sub>O. However, the incorporation of the Au atom significantly enhances WTe<sub>2</sub> adsorption capabilities. Decorating WTe<sub>2</sub> with Au atom notably augments the monolayer's capacity to adsorb gas molecules, with increasing adsorption hierarchy arranged as follows: C<sub>2</sub>H<sub>5</sub>OH > C<sub>7</sub>H<sub>8</sub> > H<sub>2</sub>O > CH<sub>2</sub>O > CO<sub>2</sub> > CH<sub>4</sub>O > C<sub>3</sub>H<sub>6</sub>O as summarized in Table 1.

**3.3.1 Adsorption and electronic properties of C<sub>7</sub>H<sub>8</sub> onto Au-WTe<sub>2</sub>.** After optimization C<sub>7</sub>H<sub>8</sub>, it is evident that gas molecules predominantly favor adsorption on Au-WTe<sub>2</sub> *via* C atoms. Gas molecules adsorbed parallel to the surface of Au-WTe<sub>2</sub> with adsorption energy ( $E_{\text{ads}}$ ) amounting to -0.55 eV as illustrated in Fig. 3(a). These shift results are significantly higher than C<sub>7</sub>H<sub>8</sub>/WTe<sub>2</sub>, as seen in Table 1. Post-optimization, the bond distance between Au and gas atoms is 3.90 Å which indicates weak interaction because the distance is greater than 3 Å.<sup>52</sup>

The electronic properties of Au-WTe<sub>2</sub> during C<sub>7</sub>H<sub>8</sub> adsorption are illustrated in Fig. 3(b). TDOS analysis shows that adsorbed gas does not affect the material's metallic behavior, indicating that Au plays a more significant role in determining metallic qualities than the influence of gas. PDOS also reveals that C-2p and H-1s orbitals overlap with Au-5d, and 6s orbitals at -0.3 eV and 1.3 eV also strong hybridization is seen in the valence band.

The results of the Hirshfeld charge analysis, shown in Fig. 10, indicate that C<sub>7</sub>H<sub>8</sub> acts as an acceptor during the adsorption process. The white and brown hues observed on C<sub>7</sub>H<sub>8</sub> indicate localized electron regions, highlighting the presence of covalent bonds between carbon and hydrogen atoms within C<sub>7</sub>H<sub>8</sub>, as illustrated in Fig. 3(c). On Au-WTe<sub>2</sub>, the

red color reflects areas of elevated electron density or localization, implying a robust interaction between Au atoms and WTe<sub>2</sub>. This suggests a mix of covalent bonding within C<sub>7</sub>H<sub>8</sub> and the possibility of metallic bonding between Au and WTe<sub>2</sub> in adsorbed configuration.

**3.3.2 Adsorption and electronic properties of CH<sub>2</sub>O onto Au-WTe<sub>2</sub>.** Adsorption of CH<sub>2</sub>O on Au-WTe<sub>2</sub> monolayer is depicted in Fig. 4(a), revealing a notable distance of 2.694 Å between Au and a carbon (C) atom showcasing a parallel tilted positioning. Despite the improvement in ( $E_{\text{ads}}$ ) of CH<sub>2</sub>O/Au-WTe<sub>2</sub> is -0.24 eV compared to CH<sub>2</sub>O/WTe<sub>2</sub> with a calculated  $E_{\text{ads}}$  of -0.01 eV, it is inferred that the presence of Au decoration minimally impacts the adsorption performance of WTe<sub>2</sub> monolayer concerning CH<sub>2</sub>O molecules.

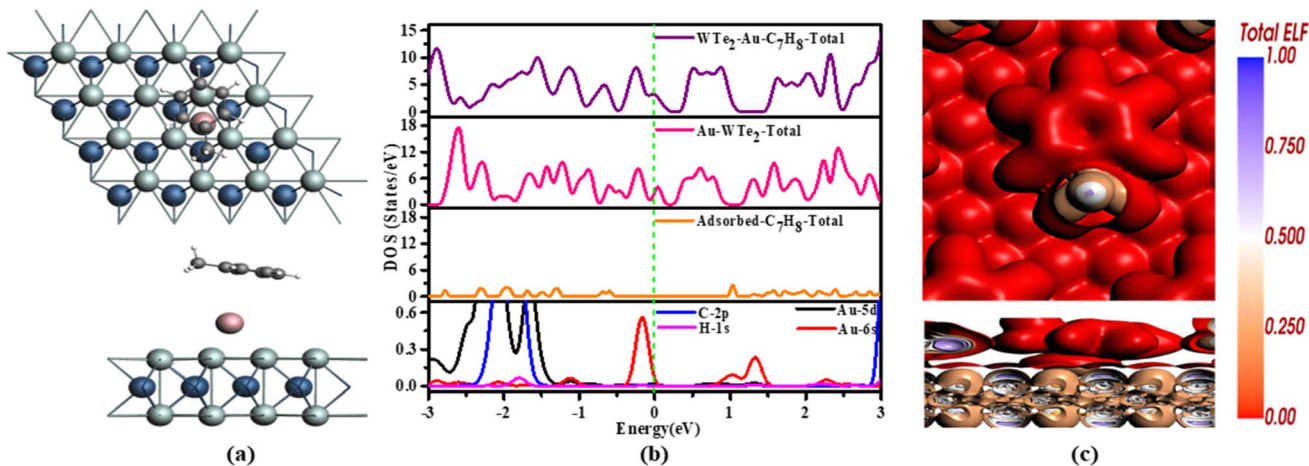
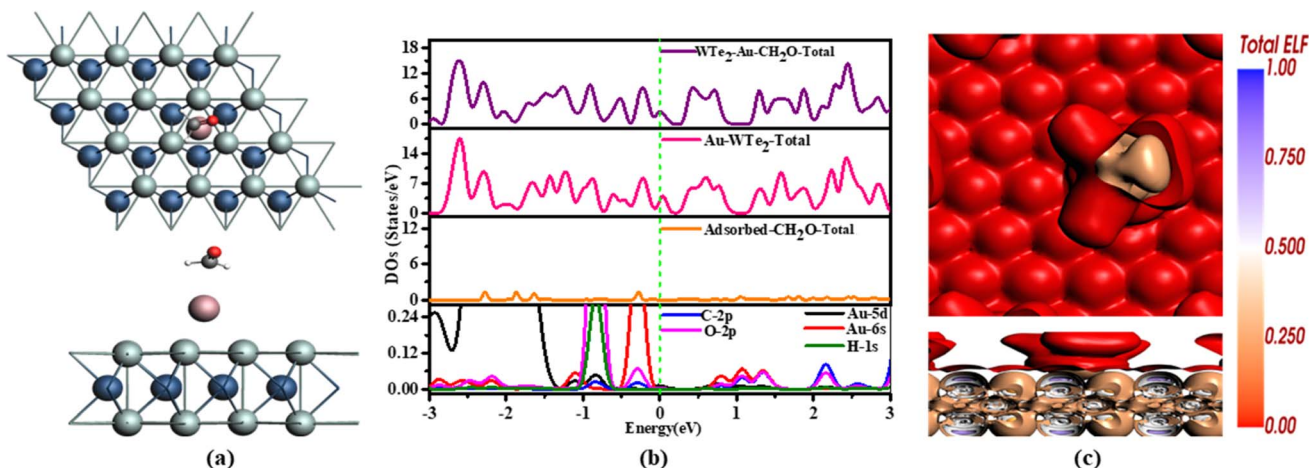
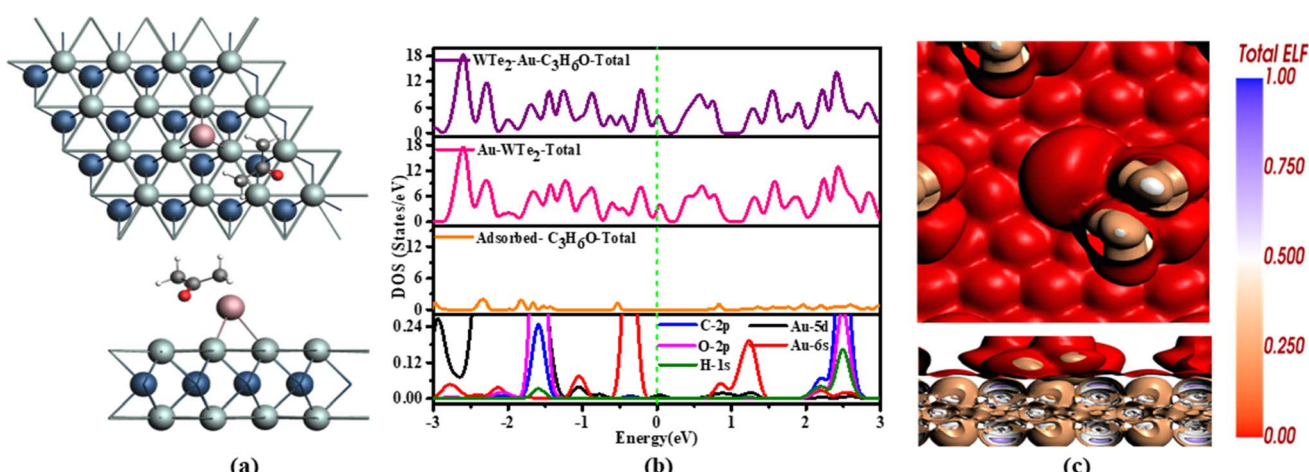
After adsorption, Au-WTe<sub>2</sub> material acts as a donor while CH<sub>2</sub>O functions as an acceptor. It is noticeable that the oxygen atom closest to the Au atom shows a subtle interaction with Au-WTe<sub>2</sub>, while the carbon atom displays some extent of charge transfer with an oxygen atom, acting as a donor, as depicted in Fig. 10.

Investigation of CH<sub>2</sub>O adsorption on an Au-WTe<sub>2</sub> entails DOS examination. PDOS interaction between Au-5d, 6s and C-2p, O-2p, and H-1s orbitals overlap at -0.3 eV and 2.1 eV and strong hybridization can be seen at -0.3 to -1.2 eV while (TDOS) overlap with Au and CH<sub>2</sub>O/Au-WTe<sub>2</sub> at 2.4 eV is illustrated in Fig. 4(b). However, peaks of adsorbed CH<sub>2</sub>O near the Fermi level indicate weak adsorption, contrasting with Au robust interactions. While CH<sub>2</sub>O/Au-WTe<sub>2</sub> displays metallic behavior, the adsorbed gas lacks this trait, suggesting Au predominantly drives the material's metallic properties rather than the adsorbed gas contribution.

Color-coded representation provided by ELF highlights specific electron densities, with brown shading on CH<sub>2</sub>O indicating the presence of pi-electron density associated with its pi-system. This observation suggests a potential for pi-interactions with Au-WTe<sub>2</sub>. Additionally, red coloring observed on Au-WTe<sub>2</sub> points to electron localization resulting from gas interaction, implying a chemical interaction and electron redistribution at the surface is illustrated in Fig. 4(c).

**3.3.3 Adsorption and electronic properties of C<sub>3</sub>H<sub>6</sub>O onto Au-WTe<sub>2</sub>.** After optimization of C<sub>3</sub>H<sub>6</sub>O on the surface of Au-WTe<sub>2</sub>, the C<sub>3</sub>H<sub>6</sub>O appeared as almost parallel and the bond distance between Au-H atoms increased from 2.927 to 3.029 Å indicating elevated physisorption<sup>16,52</sup> illustrated in Fig. 5(a).



Fig. 3 (a) Configuration of  $\text{C}_7\text{H}_8$  adsorption (b) TDOS and PDOS (c) ELF of  $\text{C}_7\text{H}_8$ .Fig. 4 (a) Adsorption configuration of  $\text{CH}_2\text{O}$  (b) TDOS and PDOS (c) ELF of  $\text{CH}_2\text{O}$ .Fig. 5 (a) Configuration of  $\text{C}_3\text{H}_6\text{O}$  adsorption (b) TDOS and PDOS (c) ELF of  $\text{C}_3\text{H}_6\text{O}$ .

This arrangement leads to an acetone adsorption energy of  $-0.08$  eV, which is strong compared to  $\text{C}_3\text{H}_6\text{O}/\text{WTe}_2$ , which can be obtained using eqn (2).

Fig. 5(b) indicates the DOS distribution of  $\text{C}_3\text{H}_6\text{O}$ . We can affirm limited contact between  $\text{C}_3\text{H}_6\text{O}$  and  $\text{Au}-\text{WTe}_2$  signifying minimal charge transfer during adsorption and showing

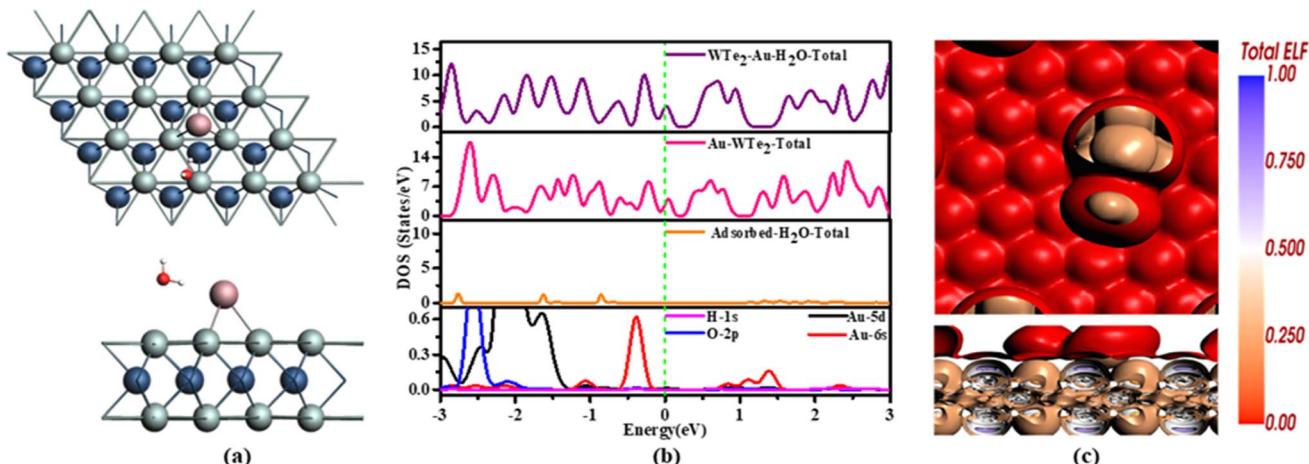


Fig. 6 (a) Configuration of  $\text{H}_2\text{O}$  adsorption (b) TDOS and PDOS (c) ELF of  $\text{H}_2\text{O}$ .

metallic behavior due to less contribution of gas molecules. Furthermore, PDOS orbital overlap very strongly at 2.2 eV and hybridization at 2.1 to 2.7 eV especially Au-5d overlap at the Fermi level. Only a discernible change in TDOS at 2.2 eV for  $\text{C}_3\text{H}_6\text{O}/\text{Au-WTe}_2$  compared to  $\text{Au-WTe}_2$ , slight elevation of peaks, and noticeable hybridization at  $-0.3$  to  $-2.4$  eV in PDOS orbitals.

Hirshfeld charge analysis indicates gas molecules exhibit an electron-accepting behavior, while  $\text{Au-WTe}_2$  serves as a donor. In the  $\text{C}_3\text{H}_6\text{O}$  system,  $\text{Au-WTe}_2$  demonstrates a robust electron-donating propensity upon gas adsorption, thereby affirming its exceptional chemical activity and reactivity in gas interaction scenarios.

Fig. 5(c) illustrates ELF Within  $\text{C}_3\text{H}_6\text{O}$ , white regions signify areas of lower electron densities, whereas brown regions denote specific electron densities like pi-electron, localized electron distributions, or distinctive bonding features within  $\text{C}_3\text{H}_6\text{O}$  molecule. The red hue on the  $\text{Au-WTe}_2$  sheet indicates particular electron distributions or localized densities on this surface. This suggests electron localization stemming from interactions between surface Au and adsorbed acetone molecule respectively.

**3.3.4 Adsorption and electronic properties of  $\text{H}_2\text{O}$  onto  $\text{Au-WTe}_2$ .** Before optimization oxygen atom is sited vertically at Au but after adsorption  $\text{H}_2\text{O}$  is inclined to the  $\text{Au-WTe}_2$  surface as illustrated in Fig. 6(a). Corresponding Au with H-atom bond length before and after are 763, and 2.387 Å respectively. This decrease in bond length suggests that the optimized configuration is more stable, with potentially stronger interactions between  $\text{H}_2\text{O}/\text{Au-WTe}_2$  due to elevated physisorption this arrangement leads to an  $\text{H}_2\text{O}$  adsorption energy of  $-0.28$  eV, which is strong as compared to  $\text{H}_2\text{O}/\text{WTe}_2$ .

$\text{Au-WTe}_2$  demonstrates electron transfer behavior, while  $\text{H}_2\text{O}$  acts as an acceptor by withdrawing electrons from a substrate, indicating a strong accepting property. It becomes evident that the oxygen atom exhibits a weak interaction with  $\text{Au-WTe}_2$ , while the hydrogen atom displays some degree of charge transfer with an oxygen atom, behaving as a donor.  $\text{WTe}_2$  suggests minimal charge transfer from a surface to adsorbed gas.

DOS distribution in Fig. 6(b) demonstrates electronic changes in the  $\text{Au-WTe}_2$  system upon  $\text{H}_2\text{O}$  adsorption. In  $\text{H}_2\text{O}$ , the peak at the Fermi level weakens, while new peaks emerge around  $-0.3$  eV and  $-0.9$  eV. A significant decrease in the PDOS

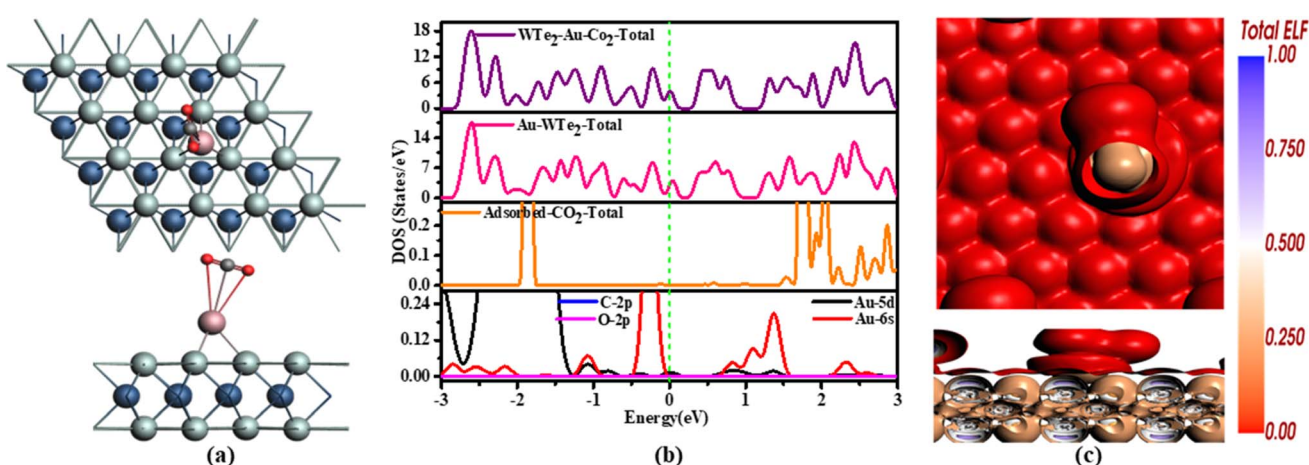


Fig. 7 (a) Configuration of  $\text{CO}_2$  adsorption (b) TDOS and PDOS (c) ELF of  $\text{CO}_2$ .



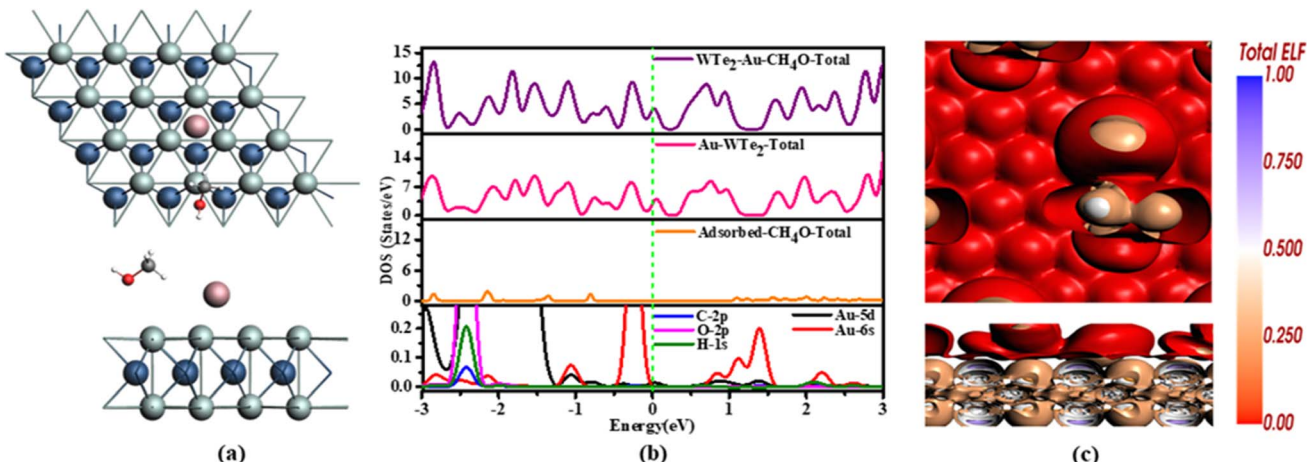


Fig. 8 (a) Configuration of CH<sub>4</sub>O adsorption (b) TDOS and PDOS (c) ELF of CH<sub>4</sub>O.

peak of Au-5d at the Fermi level provides compelling evidence compared to the isolated Au-WTe<sub>2</sub> system. Moreover, the emergence of a novel peak in PDOS around 1.5 eV due to H<sub>2</sub>O suggests hybridization with Au-5d.

ELF analysis suggests strong electron localization on both Au-WTe<sub>2</sub> sheets and adsorbed water molecules. ELF values on Au-WTe<sub>2</sub> sheets indicate strong electron localization in these regions. Brown coloring on hydrogen and oxygen atoms signifies high ELF values, indicating localized electron density around these atoms which is illustrated in Fig. 6(c).

**3.3.5 Adsorption and electronic properties of CO<sub>2</sub> onto Au-WTe<sub>2</sub>.** After the optimization configuration of CO<sub>2</sub> indicating physisorption with  $E_{\text{ads}} = -0.14$  eV, and bond length 2.45 Å that is related to the previous report.<sup>41</sup> These observed changes provide compelling evidence for the activation of both CO<sub>2</sub> and Au-WTe<sub>2</sub> during the adsorption process which is illustrated in Fig. 7(a).

The DOS analysis of CO<sub>2</sub> emphasizes the pivotal role of Au-5d orbitals in electron transfer, increasing electron density and surface electronegativity seen in Fig. 7(b). These peaks consistently align at 0 eV, indicating substantial electron transfer. Conversely, Au-6s orbitals show minimal change, maintaining their position at -1.2 eV suggesting limited involvement in electron transfer during the adsorption mechanism indicating that both Au and the gas contribute to electron transfer, playing a key role in imparting metallic properties to the material.

Hirshfeld charge analysis indicates that during the adsorption process of CO<sub>2</sub>, functions as an acceptor in this particular arrangement from Au-WTe<sub>2</sub> and Au-decorating WTe<sub>2</sub> emphasizing notable electron-donating characteristics. At the same time, the carbon atom donates a charge of 0.266e to an oxygen atom.

ELF in CO<sub>2</sub> that is illustrated in Fig. 7(c) red color on Au might designate a durable interaction between gold and WTe<sub>2</sub> and lead to a stronger interaction compared to purely metallic bonding. Analysis shows brown hues on CO<sub>2</sub>, indicating specific electron densities associated with their pi-electron systems.

**3.3.6 Adsorption and electronic properties of CH<sub>4</sub>O onto Au-WTe<sub>2</sub>.** The CH<sub>4</sub>O adsorbs on Au-WTe<sub>2</sub>, with a preference

parallel to the Au site. This configuration shows physisorption with  $E_{\text{ads}} = -0.11$  eV and 2.387 Å bond length with Au-H, indicating activation of both VOC molecules and Au-WTe<sub>2</sub> as shown in Fig. 8(a).

TDOS configuration of Au-WTe<sub>2</sub> is changed after gas adsorption. Au-WTe<sub>2</sub> peak shift to the higher region nearly close to Fermi level but after a gas adsorbed shift at Fermi level with same height and analysis show that adsorbed gas has no effect on material's metallic behavior, indicating that Au plays a more significant role in determining material's metallic qualities and PDOS interaction between Au-5d, 6s and C-2p, O-2p, H-1s orbitals overlapped at -2.4 eV and hybridized at 0.6 to 1.5 eV and -0.3 to -1.2 eV is illustrated in Fig. 8(b).

Hirshfeld charge analysis suggests that during the adsorption process, CH<sub>4</sub>O acts as an acceptor within this specific arrangement involving Au-decorated WTe<sub>2</sub>, highlighting its significant electron-donating properties. Simultaneously, the carbon atom exhibits an electron-withdrawing effect on hydrogen and oxygen atoms within the molecule.

ELF of CH<sub>4</sub>O shows metallic interaction between gold atoms, possibly forming metal-metal bonds within the gold. Additionally, there might be some sort of interaction between the gas atoms and the material, possibly involving charge transfer or electronic transitions between the gas atoms and the material's orbitals illustrated in Fig. 8(c).

**3.3.7 Adsorption and electronic properties of C<sub>2</sub>H<sub>5</sub>OH onto Au-WTe<sub>2</sub>.** Fig. 9(a) depicts the adsorption arrangement of the C<sub>2</sub>H<sub>5</sub>OH system on Au-WTe<sub>2</sub>. The C<sub>2</sub>H<sub>5</sub>OH molecule optimized on Au-WTe<sub>2</sub> in tilt form and slightly perpendicular to interact with the Au atom after optimization. This orientation is preferred due to its enhanced stability and stronger interactions, as indicated by the decrease in bond lengths between Au and the H-atom of the gas from 2.375 Å to 2.371 Å post-optimization. This decrease indicates a more stable configuration and suggests potentially stronger interactions between the molecule and the surface.<sup>25</sup> Strong interaction between the gas molecule and the adsorbent surface induces significant deformation in the geometric structure of Au-WTe<sub>2</sub>, resulting in



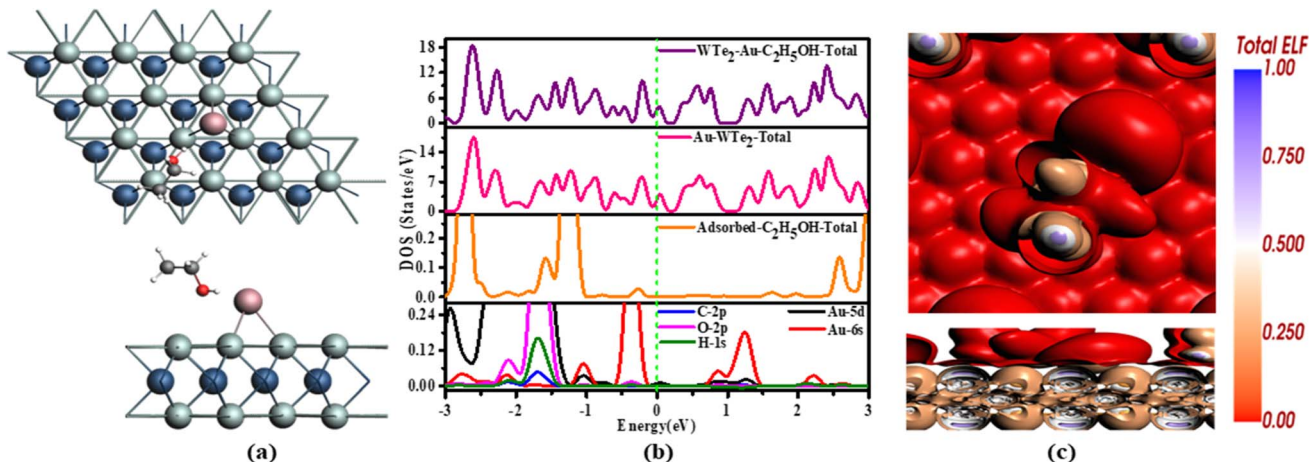


Fig. 9 (a) Configuration of C<sub>2</sub>H<sub>5</sub>OH adsorption (b) TDOS and PDOS (c) ELF of C<sub>2</sub>H<sub>5</sub>OH.

a high  $E_{\text{ads}}$  of  $-0.57$  eV, stronger than other gases and C<sub>2</sub>H<sub>5</sub>OH/WTe<sub>2</sub> interactions,<sup>29,53</sup> the Au-WTe<sub>2</sub> system demonstrates superior interaction strength and also changes electronic configuration that is roughly related to the previous report.<sup>54</sup> This enhanced adsorption energy suggests that the Au decoration significantly improves the material's sensitivity and effectiveness for detecting C<sub>2</sub>H<sub>5</sub>OH, making it a more promising candidate for sensor applications.

C<sub>2</sub>H<sub>5</sub>OH demonstrates an accepting nature, while the Au-WTe<sub>2</sub> material serves as a donating behavior. Au-decorated WTe<sub>2</sub> exhibits a strong capability for electron donation upon the adsorption of C<sub>2</sub>H<sub>5</sub>OH. This emphasizes its notable chemical activity and reactivity in gas interaction scenarios as in Fig. 10.

TDOS, giving rise to innovative peaks in DOS of C<sub>2</sub>H<sub>5</sub>OH structure. This deformation leads to the disintegration of electronic states around the Fermi level into quite a few smaller states around 2.1 eV and at  $-0.3$  eV. From PDOS we can see the hybridization of C-2p, O-2p, H-1s, and Au 5d, 6s orbitals in the range from  $-2.3$  eV to 1.4 eV as depicted in Fig. 9(b). Similar to observations in the system, it is evident that TDOS of the C<sub>2</sub>H<sub>5</sub>OH system has an activated peak at the Fermi level that indicates metallic behavior of C<sub>2</sub>H<sub>5</sub>OH/Au-WTe<sub>2</sub> similar to Au-decorated WTe<sub>2</sub>. This analysis highlights the profound impact

of Au-WTe<sub>2</sub> interaction on electronic structure, with implications for the adsorption characteristics of C<sub>2</sub>H<sub>5</sub>OH on the surface.

ELF, a computational tool, unveils electron distributions, facilitating the comprehension of chemical bonds and interactions by displaying varied colors. Brown hues on C<sub>2</sub>H<sub>5</sub>OH indicate specific electron densities related to their pi-electron systems, hinting at potential pi-interactions with the Au-decorated WTe<sub>2</sub> surface. Conversely, red coloring on Au-WTe<sub>2</sub> denotes electron localization due to interactions with the adsorbed gas, suggesting the emergence of chemical interactions illustrated in Fig. 9(c).

## 4. Gas-sensing interpretation

### 4.1 Sensitivity and selectivity

In assessing the effectiveness of Au-decorated WTe<sub>2</sub> as a gas sensor for CH<sub>2</sub>O, C<sub>7</sub>H<sub>8</sub>, CH<sub>4</sub>O, C<sub>2</sub>H<sub>5</sub>OH, CO<sub>2</sub>, C<sub>3</sub>H<sub>6</sub>O, and H<sub>2</sub>O molecules, attention must be paid to both their adsorption characteristics and electrical conductivity. The sensor's sensitivity relies on detecting changes in conductivity resulting from variations in the bandgap. Specifically, a reduction in bandgap leads to heightened electrical conductivity. To gauge sensor performance, key metrics such as sensitivity ( $S$ ) and electrical conductivity ( $\sigma$ ) are computed, indicating the material's ability to detect gases effectively calculated by using eqn (4) and (5).<sup>25,55</sup> After adsorbing VOCs, bandgap values of Au-WTe<sub>2</sub> remain at 0 eV, indicating a potential enhancement in conductivity. This phenomenon aligns with observations in other resistance-type sensors, where increased conductivity is often noted.<sup>25,56,57</sup> Another aspect of device performance to consider is selectivity. Previous research indicated that selective detection among multiple species could be achieved by observing changes in either bandgap or conductivity.<sup>57</sup> Certain studies have utilized sensitivity ratios of specific molecules to measure selectivity. Even when adsorption energy and bandgap values are comparable across various adsorption systems, certain sensors have demonstrated remarkable selectivity.<sup>38,58</sup>

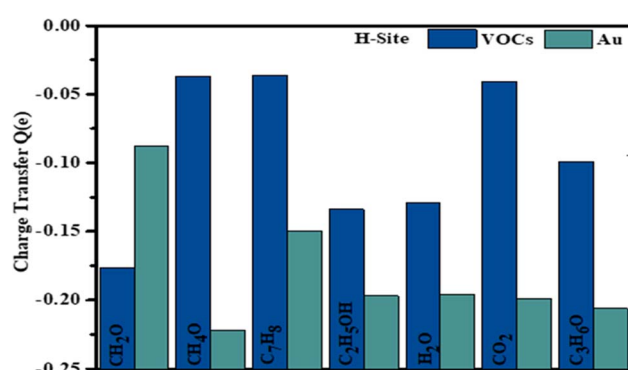


Fig. 10 Charge transfer of system.



Table 2 VOCs sensing performance on Au-decorated WTe<sub>2</sub>

VOCs molecule	Adsorption energy (eV)	Band gap (E <sub>g</sub> )	Bond length (Å)	Work function (eV)	Work function sensitivity (%)	Charge Q(e)	Sensitivity (%)
H <sub>2</sub> O	-0.28	0	2.38	3.9475	-0.49	-0.129	100
CO <sub>2</sub>	-0.14	0	2.45	4.0149	1.20	-0.041	100
CH <sub>2</sub> O	-0.24	0	2.69	4.2326	6.69	-0.177	100
CH <sub>4</sub> O	-0.11	0	2.38	3.7956	-4.30	-0.037	100
C <sub>7</sub> H <sub>8</sub>	-0.55	0	3.90	3.8839	-2.09	-0.036	100
C <sub>3</sub> H <sub>6</sub> O	-0.08	0	3.02	3.8215	-3.66	-0.099	100
C <sub>2</sub> H <sub>5</sub> OH	-0.57	0	2.37	3.9354	-0.79	-0.134	100

Table 3 Recovery time ( $\tau$ ) for mentioned VOCs at different temperatures

System	$\tau$ (s) 298 K	$\tau$ (s) 398 K	$\tau$ (s) 498 K
C <sub>2</sub> H <sub>5</sub> OH	$7.97 \times 10^{-3}$	$1.90 \times 10^{-5}$	$5.89 \times 10^{-7}$
C <sub>7</sub> H <sub>8</sub>	$3.85 \times 10^{-3}$	$1.06 \times 10^{-5}$	$1.15 \times 10^{-7}$
H <sub>2</sub> O	$7.31 \times 10^{-8}$	$3.77 \times 10^{-9}$	$6.83 \times 10^{-10}$
CO <sub>2</sub>	$2.27 \times 10^{-10}$	$6.14 \times 10^{-11}$	$2.61 \times 10^{-11}$
CH <sub>2</sub> O	$1.47 \times 10^{-8}$	$1.16 \times 10^{-9}$	$2.68 \times 10^{-10}$
CH <sub>4</sub> O	$8.14 \times 10^{-11}$	$2.54 \times 10^{-11}$	$1.29 \times 10^{-11}$
C <sub>3</sub> H <sub>6</sub> O	$2.4 \times 10^{-11}$	$1.04 \times 10^{-11}$	$6.4 \times 10^{-12}$

With a bandgap of 0 eV across all VOCs, adsorbed systems exhibit a sensitivity of 100% for each gas which can be seen in Table 2. This implies that high sensitivity and selectivity are anticipated for qualitatively detecting VOCs through conductivity and selectivity measurements.

## 4.2 Recovery time

The recovery time ( $\tau$ ) is crucial for gas sensor effectiveness, as it indicates the detachment of gas molecules post-detection. A shorter  $\tau$  indicates superior reversibility, highlighting the efficacy of gas sensors in detecting and releasing gas molecules.<sup>39,59,60</sup> The study investigated Au-WTe<sub>2</sub> desorption at 298 K, 398 K, and 498 K, analyzing potential barrier ( $E_{\text{ads}}$ ) and recovery times as shown in Table 3. High  $E_{\text{ads}}$  in C<sub>2</sub>H<sub>5</sub>OH leads to a notable energy barrier for desorption, resulting in prolonged recovery times, like  $7.97 \times 10^{-3}$  s at 298 K. Conversely, C<sub>3</sub>H<sub>6</sub>O, the smallest  $E_{\text{ads}}$ , desorbs easily from the Au-WTe<sub>2</sub>, with desorption times of  $2.4 \times 10^{-11}$  s at 298 K,  $1.04 \times 10^{-11}$  s at 398 K, and  $6.4 \times 10^{-12}$  s at 498 K. As the working temperature increases, the recovery time of Au-WTe<sub>2</sub> towards VOCs decreases, especially evident in C<sub>2</sub>H<sub>5</sub>OH desorption, where time reduces to  $5.89 \times 10^{-7}$  s at 498 K.

We assert that Au-WTe<sub>2</sub> shows promising material for the detection of C<sub>2</sub>H<sub>5</sub>OH. This is due to its consistent adsorption performance at ambient temperature and rapid recovery time at high temperatures, facilitating its repeated and efficient use. However, the remarkably short recovery time observed for the C<sub>3</sub>H<sub>6</sub>O desorption system at 298 K and 498 K indicates that Au-WTe<sub>2</sub> is unsuitable for use as a sensor for C<sub>3</sub>H<sub>6</sub>O. The adsorption and desorption performance of Au-WTe<sub>2</sub> for H<sub>2</sub>O molecules at ambient temperature indicates its suitability as a water sensor under simple operating conditions.<sup>55</sup>

## 4.3 Work function

Adsorption of VOCs typically alters a material's work function, which is a crucial parameter in gas detection applications.<sup>61,62</sup> The work function represents the energy required to move an electron from the Fermi level to the vacuum and is calculated by eqn (7). Alterations in the work function of a system significantly impact its electrical conductivity. The intrinsic work function of pure WTe<sub>2</sub> is 3.42 eV, while Au-WTe<sub>2</sub> has 3.96 eV. Upon adsorption of CO<sub>2</sub>, H<sub>2</sub>O, CH<sub>4</sub>O·C<sub>2</sub>H<sub>5</sub>OH, CH<sub>2</sub>O, C<sub>3</sub>H<sub>6</sub>O, C<sub>7</sub>H<sub>8</sub> the work function changes. Work functions (WFs) of CH<sub>2</sub>O and CO<sub>2</sub> systems increase to 4.23 and 4.01 eV. Consequently, CH<sub>4</sub>O adsorption leads to a significant decrease in work function compared to other gases.<sup>63,64</sup> It's important to note that DFT calculations can reasonably predict the changes in work function induced by physisorbed gases.<sup>63</sup> Experimentally, the change in work function due to gas adsorption is estimated using the Scanning Kelvin Probe, enabling the development of work function-based gas sensors. The work functions of pristine WTe<sub>2</sub> and Au-WTe<sub>2</sub> are 3.42 and 3.96 eV, respectively, suggesting weaker electron affinity compared to graphene and Ni-doped WTe<sub>2</sub>, and heightened potential for vacuum-level electron release.<sup>40,65-67</sup> The formula to calculate the sensitivity of the work function of Au-WTe<sub>2</sub> with gases is.<sup>68-70</sup>

$$S = \left| \frac{\Phi_{\text{gas}} - \Phi_{\text{Au-WTe}_2}}{\Phi_{\text{Au-WTe}_2}} \right| \times 100\%$$

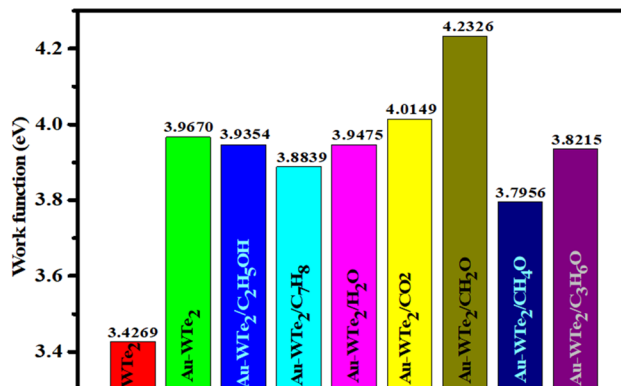


Fig. 11 Comparative analysis of work function for WTe<sub>2</sub> and Au-decorated WTe<sub>2</sub> before and after exposure to volatile organic compounds (VOCs).



The equation can be utilized to determine the sensitivity of the work function. Where  $\Phi_{\text{gas}}$  and  $\Phi_{\text{Au-WTe}_2}$  represent the work function of systems with gases adsorbed respectively. These findings show varied trends in the work function of  $\text{CH}_2\text{O}$  and  $\text{CO}_2$  systems. It increases to 4.23 and 4.01 eV with the sensitivity of work-function 6.69% and 1.20% respectively as shown in Fig. 11.

In contrast, other gases such as  $\text{C}_3\text{H}_6\text{O}$ ,  $\text{H}_2\text{O}$ ,  $\text{C}_7\text{H}_8$ ,  $\text{C}_2\text{H}_5\text{OH}$ , and  $\text{CH}_4\text{O}$  exhibit decreases in WF of  $-3.66$ ,  $-0.49$ ,  $-2.09$ ,  $-0.79$  and  $-4.3\%$ , respectively than  $\text{Au-WTe}_2$ . The work function-based  $\text{Au-WTe}_2$  sensor shows high sensitivity towards  $\text{CH}_2\text{O}$  compared to other gases. This is attributed to the higher Fermi energy of  $\text{CH}_2\text{O}$  compared to gases, resulting in a higher work function. As a result,  $\text{CH}_2\text{O}$  exhibits greater sensitivity as it requires less energy for electrons to escape from the Fermi level to infinity than other gases.

## 5. Conclusion

Nanosensors offer a cost-effective and non-invasive approach to early lung cancer detection. A key challenge is designing breath sensors that selectively detect specific biomarkers. In this study, the sensing capability of Au-decorated  $\text{WTe}_2$  for volatile organic compounds like acetone, ethanol, methanol, formaldehyde, and toluene commonly associated with lung cancer biomarkers, was assessed using DFT calculations. Additionally, we studied interfering gases commonly present in exhaled breath, specifically carbon dioxide and water. Our calculations indicate that the pristine  $\text{WTe}_2$  monolayer exhibits limited adsorption of the target molecules rendering it unsuitable for lung cancer detection. The Au-decoration increases the adsorption strength of VOC molecules on the  $\text{WTe}_2$  monolayer surface, extending their recovery periods to the detectable range. After accounting for the adsorption distances and charge transfers of the related VOCs, the adsorption onto the  $\text{Au-WTe}_2$  surface is primarily physisorption. Furthermore, we analyzed desorption patterns and sensing mechanisms of  $\text{Au-WTe}_2$  concerning VOCs. Au adsorbed onto  $\text{WTe}_2$  via H-sites, and electronic properties of  $\text{Au-WTe}_2$  remain unchanged following interaction with gases.  $\text{Au-WTe}_2$  demonstrates promising potential as a sensing material for VOC molecules due to its effective adsorption and desorption capabilities under specific conditions. The work function-based  $\text{Au-WTe}_2$  sensor shows high sensitivity towards  $\text{CH}_2\text{O}$  compared to other gases with 6.69% respectively. However, it excels in detecting ethanol vapor molecules, making it a promising option for accurately assessing operational efficiency. We expect that the findings of this study will contribute to the development of effective  $\text{Au-WTe}_2$ -based nanosensors for early lung cancer detection by targeting specific VOCs.

## Data availability

All data generated or analyzed during this study are included in this published article.

## Conflicts of interest

The authors declare no conflict of interest.

## Acknowledgements

Authors express their appreciation to the Deanship of Scientific Research at King Khalid University, Saudi Arabia, for funding this work through a research group program under grant number RGP 2/538/45 to Saleh S Alarfaj.

## References

- 1 A. W. Boots, J. J. van Berk, J. W. Dallinga, A. Smolinska, E. F. Wouters and F. J. van Schooten, The versatile use of exhaled volatile organic compounds in human health and disease, *J. Breath Res.*, 2012, **6**(2), 027108.
- 2 Y. Y. Broza and H. Haick, Nanomaterial-based sensors for detection of disease by volatile organic compounds, *Nanomedicine*, 2013, **8**(5), 785–806.
- 3 S. Sun, T. Hussain, W. Zhang and A. Karton, Blue phosphorene monolayers as potential nano sensors for volatile organic compounds under point defects, *Appl. Surf. Sci.*, 2019, **486**, 52–57.
- 4 B. de Lacy Costello, A. Amann, H. Al-Kateb, C. Flynn, W. Filipiak, T. Khalid, D. Osborne and N. M. Ratcliffe, A review of the volatiles from the healthy human body, *J. Breath Res.*, 2014, **8**(1), 014001.
- 5 X. Sun, K. Shao and T. Wang, Detection of volatile organic compounds (VOCs) from exhaled breath as noninvasive methods for cancer diagnosis, *Anal. Bioanal. Chem.*, 2016, **408**, 2759–2780.
- 6 T. Hibbard and A. J. Killard, Breath ammonia analysis: clinical application and measurement, *Crit. Rev. Anal. Chem.*, 2011, **41**(1), 21–35.
- 7 S. Das and M. Pal, Non-invasive monitoring of human health by exhaled breath analysis: a comprehensive review, *J. Electrochem. Soc.*, 2020, **167**(3), 037562.
- 8 Z. Cheng, B. Li, W. Yu, H. Wang, T. Zhang, J. Xiong and Z. Bu, Risk assessment of inhalation exposure to VOCs in dwellings in Chongqing, China, *Toxicol. Res.*, 2018, **7**(1), 59–72.
- 9 D. Zhang, Q. Mi, D. Wang and T. Li, MXene/Co<sub>3</sub>O<sub>4</sub> composite based formaldehyde sensor driven by ZnO/MXene nanowire arrays piezoelectric nanogenerator, *Sens. Actuators, B*, 2021, **339**, 129923.
- 10 X. Shao, D. Zhang, M. Tang, H. Zhang, Z. Wang, P. Jia and J. Zhai, Amorphous Ag catalytic layer-SnO<sub>2</sub> sensitive layer-graphite carbon nitride electron supply layer synergy-enhanced hydrogen gas sensor, *Chem. Eng. J.*, 2024, 153676.
- 11 H. Zhang, D. Zhang, R. Mao, L. Zhou, C. Yang, Y. Wu, Y. Liu and Y. Ji, MoS<sub>2</sub>-based charge trapping layer enabled triboelectric nanogenerator with assistance of CNN-GRU model for intelligent perception, *Nano Energy*, 2024, **127**, 109753.
- 12 H. Zhang, D.-Z. Zhang, D.-Y. Wang, Z.-Y. Xu, Y. Yang and B. Zhang, Flexible single-electrode triboelectric nanogenerator with MWCNT/PDMS composite film for environmental energy harvesting and human motion monitoring, *Rare Met.*, 2022, **41**(9), 3117–3128.
- 13 S. Wang, J. Wang, Y. Zhu, J. Yang and F. Yang, A new device for liver cancer biomarker detection with high accuracy, *Sens. Bio-Sens. Res.*, 2015, **4**, 40–45.



14 N. Peled, O. Barash, U. Tisch, R. Ionescu, Y. Y. Broza, M. Ilouze, J. Mattei, P. A. Bunn Jr, F. R. Hirsch and H. Haick, Volatile fingerprints of cancer specific genetic mutations, *Nanomed. Nanotechnol. Biol. Med.*, 2013, **9**(6), 758–766.

15 N. Nasiri and C. Clarke, Nanostructured chemiresistive gas sensors for medical applications, *Sensors*, 2019, **19**(3), 462.

16 R. P. Reji, S. K. C. Balaji, Y. Sivalingam, Y. Kawazoe and S. Velappa Jayaraman, First-principles density functional theory calculations on the potential of  $\text{Sc}_2\text{CO}_2$  MXene nanosheets as a dual-mode sensor for detection of volatile organic compounds in exhaled human breath, *ACS Appl. Nano Mater.*, 2023, **6**(7), 5345–5356.

17 K. Timsina and S. Lepcha, MSc thesis, Sikkim Manipal Institute of Technology, 2022.

18 J. Gusakova, X. Wang, L. L. Shiau, A. Krivosheeva, V. Shaposhnikov, V. Borisenko, V. Gusakov and B. K. Tay, Electronic properties of bulk and monolayer TMDs: theoretical study within DFT framework (GVJ-2e method), *Phys. Status Solidi A*, 2017, **214**(12), 1700218.

19 X. Huang, Z. Zeng and H. Zhang, Metal dichalcogenide nanosheets: preparation, properties and applications, *Chem. Soc. Rev.*, 2013, **42**(5), 1934–1946.

20 L. Margulis, G. Salitra, R. Tenne and M. Talianker, Nested fullerene-like structures, *Nature*, 1993, **365**(6442), 113–114.

21 R. Frindt and A. Yoffe, Physical properties of layer structures: optical properties and photoconductivity of thin crystals of molybdenum disulphide, *Proc. R. Soc. Lond., Ser. A, Math. Phys. Sci.*, 1963, **273**(1352), 69–83.

22 M. I. Khan, A. Saeed, M. Shakil, G. Saira, A. Ahmad, F. Imam and S. S. Alarfaji, Computational exploration of high-capacity hydrogen storage in alkali metal-decorated  $\text{MgB}_2$  material, *J. Power Sources*, 2024, **613**, 234881.

23 A. Kononov, M. Endres, G. Abulizi, K. Qu, J. Yan, D. G. Mandrus, K. Watanabe, T. Taniguchi and C. Schönenberger, Superconductivity in type-II Weyl-semimetal  $\text{WTe}_2$  induced by a normal metal contact, *J. Appl. Phys.*, 2021, **129**, 113903.

24 B. Amin, T. P. Kaloni and U. Schwingenschlögl, Strain engineering of  $\text{WS}_2$ ,  $\text{WSe}_2$ , and  $\text{WTe}_2$ , *RSC Adv.*, 2014, **4**(65), 34561–34565.

25 Y. Liu, L. Gao, S. Fu, S. Cheng, N. Gao and H. Li, Highly efficient VOC gas sensors based on Li-doped diamane, *Appl. Surf. Sci.*, 2023, **611**, 155694.

26 V. Nagarajan and R. Chandiramouli,  $\text{MoSe}_2$  nanosheets for detection of methanol and ethanol vapors: a DFT study, *J. Mol. Graphics Modell.*, 2018, **81**, 97–105.

27 F. Li, F. Chen, H. Cui and X. Jiang, Pristine and Ni-doped  $\text{WTe}_2$  monolayer for adsorption and sensing of  $\text{C}_2\text{H}_2$  and  $\text{C}_2\text{H}_4$  in oil-immersed transformers: a DFT study, *Comput. Theor. Chem.*, 2023, **1226**, 114187.

28 Z. Xu, H. Cui and G. Zhang, Pd-decorated  $\text{WTe}_2$  monolayer as a favorable sensing material toward  $\text{SF}_6$  decomposed species: a DFT study, *ACS Omega*, 2023, **8**(4), 4244–4250.

29 F. Huang, T.-Y. Sang, X. Hu, Z. Wang and W. Chen, Adsorption behaviors and electronic properties of Pd-doped  $\text{MoTe}_2$  monolayer for hazardous gases detecting and scavenging, *Mater. Sci. Semicond. Process.*, 2024, **170**, 107920.

30 L. Li, Z.-W. Tian, W.-H. Zhao, Q.-C. Zheng and R. Jia, Sniff lung cancer biomarkers in breath using N-doped monolayer  $\text{WS}_2$ : a theoretical feasibility, *Appl. Surf. Sci.*, 2023, **614**, 156257.

31 G. t. Te Velde, F. M. Bickelhaupt, E. J. Baerends, C. Fonseca Guerra, S. J. van Gisbergen, J. G. Snijders and T. Ziegler, Chemistry with ADF, *J. Comput. Chem.*, 2001, **22**(9), 931–967.

32 M. Güell, J. M. Luis, M. Sola and M. Swart, Importance of the basis set for the spin-state energetics of iron complexes, *J. Phys. Chem. A*, 2008, **112**(28), 6384–6391.

33 E. Van Lenthe and E. J. Baerends, Optimized Slater-type basis sets for the elements 1–118, *J. Comput. Chem.*, 2003, **24**(9), 1142–1156.

34 J. P. Perdew, K. Burke and M. Ernzerhof, Generalized gradient approximation made simple, *Phys. Rev. Lett.*, 1996, **77**(18), 3865.

35 S. Grimme, Semiempirical GGA-type density functional constructed with a long-range dispersion correction, *J. Comput. Chem.*, 2006, **27**(15), 1787–1799.

36 M. Franchini, P. H. T. Philipsen and L. Visscher, The Becke fuzzy cells integration scheme in the Amsterdam Density Functional program suite, *J. Comput. Chem.*, 2013, **34**(21), 1819–1827.

37 R. Li, J. Zhang, S. Hou, Z. Qian, Z. Shen, X. Zhao and Z. Xue, A corrected NEGF + DFT approach for calculating electronic transport through molecular devices: filling bound states and patching the non-equilibrium integration, *Chem. Phys.*, 2007, **336**(2–3), 127–135.

38 S. Aghaei, A. Aasi, S. Farhangdoust and B. Panchapakesan, Graphene-like  $\text{BC}_6\text{N}$  nanosheets are potential candidates for detection of volatile organic compounds (VOCs) in human breath: a DFT study, *Appl. Surf. Sci.*, 2021, **536**, 147756.

39 S. Peng, K. Cho, P. Qi and H. Dai, *Ab initio* study of CNT  $\text{NO}_2$  gas sensor, *Chem. Phys. Lett.*, 2004, **387**(4–6), 271–276.

40 F. Li, F. Chen, H. Cui and X. Jiang, Pristine and Ni-doped  $\text{WTe}_2$  monolayer for adsorption and sensing of  $\text{C}_2\text{H}_2$  and  $\text{C}_2\text{H}_4$  in oil-immersed transformers: a DFT study, *Comput. Theor. Chem.*, 2023, 114187.

41 S. Ma, L. Su, L. Jin, J. Su and Y. Jin, A first-principles insight into Pd-doped  $\text{MoSe}_2$  monolayer: a toxic gas scavenger, *Phys. Lett. A*, 2019, **383**(30), 125868.

42 T. Hussain, P. Panigrahi and R. Ahuja, Enriching physisorption of  $\text{H}_2\text{S}$  and  $\text{NH}_3$  gases on a graphane sheet by doping with Li adatoms, *Phys. Chem. Chem. Phys.*, 2014, **16**(17), 8100–8105.

43 Z. Xu, B. Luo, M. Chen, W. Xie, Y. Hu and X. Xiao, Enhanced photogalvanic effects in the two-dimensional  $\text{WTe}_2$  monolayer by vacancy-and substitution-doping, *Appl. Surf. Sci.*, 2021, **548**, 148751.

44 J. B. Barot, S. K. Gupta and P. N. Gajjar, Optical properties of  $\text{WTe}_2$ -a layered topological insulator: a DFT study, *Mater. Today: Proc.*, 2023, DOI: [10.1016/j.matpr.2023.01.191](https://doi.org/10.1016/j.matpr.2023.01.191).

45 P. Cai, J. Hu, L. He, J. Pan, X. Hong, Z. Zhang, J. Zhang, J. Wei, Z. Mao and S. Li, Drastic pressure effect on the



extremely large magnetoresistance in WTe<sub>2</sub>: quantum oscillation study, *Phys. Rev. Lett.*, 2015, **115**(5), 057202.

46 N. Shehzad, I. Shahid, S. Yao, S. Ahmad, A. Ali, L. Zhang and Z. Zhou, A first-principles study of electronic structure and photocatalytic performance of two-dimensional van der Waals MTe<sub>2</sub>-As (M= Mo, W) heterostructures, *Int. J. Hydrogen Energy*, 2020, **45**(51), 27089–27097.

47 X.-Q. Tian, L. Liu, X.-R. Wang, Y.-D. Wei, J. Gu, Y. Du and B. I. Yakobson, Engineering of the interactions of volatile organic compounds with MoS<sub>2</sub>, *J. Mater. Chem. C*, 2017, **5**(6), 1463–1470.

48 L. Wang, Z. Lin, Y. Du, H. Guo, K. Zheng, J. Yu, X. Chen and L. Lang, Properties-enhanced gas sensor based on Cu-doped tellurene monolayer to detect acetone molecule: a first-principles study, *Mol. Phys.*, 2021, **119**(7), e1864490.

49 P. Ou, P. Song, X. Liu and J. Song, Superior sensing properties of black phosphorus as gas sensors: a case study on the volatile organic compounds, *Adv. Theory Simul.*, 2019, **2**(1), 1800103.

50 C.-H. Yeh, Computational study of Janus transition metal dichalcogenide monolayers for acetone gas sensing, *ACS Omega*, 2020, **5**(48), 31398–31406.

51 U. Nosheen, A. Jalil, S. Z. Ilyas, A. Illahi, S. A. Khan and A. Hassan, First-Principles Insight into a B<sub>4</sub>C<sub>3</sub> Monolayer as a Promising Biosensor for Exhaled Breath Analysis, *J. Electron. Mater.*, 2022, **51**(11), 6568–6578.

52 S. S. Dindorkar, N. Sinha and A. Yadav, Comparative study on adsorption of volatile organic compounds on graphene, boron nitride and boron carbon nitride nanosheets, *Solid State Commun.*, 2023, **359**, 115021.

53 Y. Yan, Y. Luo, Y. Li, Y. Zhang, P. Wu, J. Tang, X. Zhang and S. Xiao, Transition metal (Au, Ag, Pt, Pd, Ni) doped MoS<sub>2</sub> as gas sensing materials for C<sub>4</sub>F<sub>7</sub>N leakage detection: a comparative study, *Surf. Interfaces*, 2024, **44**, 103625.

54 Y. Yang, K. Hu, J. Zhang, T. He, Y. Jiang, Y. Zhang and H. Liu, Adsorption properties of noble-metal (Ag, Rh, or Au)-doped CeO<sub>2</sub> (1 1 0) to CO: a DFT + U study, *Comput. Mater. Sci.*, 2024, **231**, 112543.

55 H. Cui, X. Zhang, G. Zhang and J. Tang, Pd-doped MoS<sub>2</sub> monolayer: a promising candidate for DGA in transformer oil based on DFT method, *Appl. Surf. Sci.*, 2019, **470**, 1035–1042.

56 Q. Wan, X. Chen and Y. Gui, First-principles insight into a Ru-doped SnS<sub>2</sub> monolayer as a promising biosensor for exhale gas analysis, *ACS Omega*, 2020, **5**(15), 8919–8926.

57 H. Cui, P. Jia and X. Peng, Adsorption of SO<sub>2</sub> and NO<sub>2</sub> molecule on intrinsic and Pd-doped HfSe<sub>2</sub> monolayer: a first-principles study, *Appl. Surf. Sci.*, 2020, **513**, 145863.

58 A. Aasi, S. M. Aghaei and B. Panchapakesan, Pt-decorated phosphorene as a propitious room temperature VOC gas sensor for sensitive and selective detection of alcohols, *J. Mater. Chem. C*, 2021, **9**(29), 9242–9250.

59 X. Tang, A. Du and L. Kou, Gas sensing and capturing based on two-dimensional layered materials: overview from theoretical perspective, *Wiley Interdiscip. Rev.: Comput. Mol. Sci.*, 2018, **8**(4), e1361.

60 T. Liu, Z. Cui, X. Li, H. Cui and Y. Liu, Al-doped MoSe<sub>2</sub> monolayer as a promising biosensor for exhaled breath analysis: a DFT study, *ACS Omega*, 2020, **6**(1), 988–995.

61 T. Hussain, D. Singh, S. K. Gupta, A. Karton, Y. Sonvane and R. Ahuja, Efficient and selective sensing of nitrogen-containing gases by Si<sub>2</sub>BN nanosheets under pristine and pre-oxidized conditions, *Appl. Surf. Sci.*, 2019, **469**, 775–780.

62 D. Singh, P. K. Panda, Y. K. Mishra and R. Ahuja, van der Waals induced molecular recognition of canonical DNA nucleobases on a 2D GaS monolayer, *Phys. Chem. Chem. Phys.*, 2020, **22**(12), 6706–6715.

63 M.-L. Bocquet, A. Rappe and H.-L. Dai\*, A density functional theory study of adsorbate-induced work function change and binding energy: olefins on Ag (111), *Mol. Phys.*, 2005, **103**(6–8), 883–890.

64 M. Gussoni, M. Rui and G. Zerbi, Electronic and relaxation contribution to linear molecular polarizability. An analysis of the experimental values, *J. Mol. Struct.*, 1998, **447**(3), 163–215.

65 Z. Jiang, Q. Pan, M. Li, T. Yan and T. Fang, Density functional theory study on direct catalytic decomposition of ammonia on Pd (1 1 1) surface, *Appl. Surf. Sci.*, 2014, **292**, 494–499.

66 F. Li, X. Gao, R. Wang, T. Zhang and G. Lu, Study on TiO<sub>2</sub>-SnO<sub>2</sub> core-shell heterostructure nanofibers with different work function and its application in gas sensor, *Sens. Actuators, B*, 2017, **248**, 812–819.

67 D. Singh and R. Ahuja, Highly sensitive gas sensing material for environmentally toxic gases based on janus NbSeTe monolayer, *Nanomaterials*, 2020, **10**(12), 2554.

68 D. Chidambaram, R. Kalidoss, K. Pushparaj, V. J. Surya and Y. Sivalingam, Post-deposition annealing influences of gas adsorption on semi-vertical  $\beta$ -FeOOH nanorods at room temperature: a scanning kelvin probe analysis, *Mater. Sci. Eng., B*, 2022, **280**, 115694.

69 Y. Sivalingam, P. Elumalai, S. V. Yuvaraj, G. Magna, V. J. Sowmya, R. Paolesse, K.-W. Chi, Y. Kawazoe and C. Di Natale, Interaction of VOCs with pyrene tetratopic ligands layered on ZnO nanorods under visible light, *J. Photochem. Photobiol., A*, 2016, **324**, 62–69.

70 R. P. Reji, G. Marappan, Y. Sivalingam and V. J. Surya, VOCs adsorption induced surface potential changes on phthalocyanines: a combined experimental and theoretical approach towards food freshness monitoring, *Mater. Lett.*, 2022, **306**, 130945.

